


Cite this: *RSC Adv.*, 2021, **11**, 35673

Promoting the stability and adsorptive capacity of Fe_3O_4 -embedded expanded graphite with an aminopropyltriethoxysilane–polydopamine coating for the removal of copper(II) from water[†]

Shunhui Wang, ^{*a} Wenjian Lao, ^c Yi He, ^{*ab} Heng Shi, ^a Qihang Ye^a and Jing Ma^a

In this study, three magnetic graphites, namely, EGF, GAF, and GFA + KH550, were prepared, which were loaded either with Fe_3O_4 or with Fe_3O_4 and PDA or with Fe_3O_4 , PDA, and KH550 onto expanded graphite. ATR-FTIR, XRD, XPS, SEM, TEM, and TGA characterization results showed that EGF, GAF, and GFA + KH550 were successfully prepared. Under the same initial copper concentration, the removal rates of copper ions by EGF, GFA, and GFA + KH550 were 86.2%, 96.9%, and 97.0%, respectively and the hazard index reductions of the three adsorbents were 2191 ± 71 (EGF), 1843 ± 68 (GFA), and 1664 ± 102 (GFA + KH550), respectively. Therefore GFA + KH550 exhibited better removal of Cu(II) than EGF and GFA, for PDA and KH550 provided more adsorption-active sites like –OH and –NH. Here, the adsorption of GFA + KH550 fitted the pseudo-second-order kinetic and Langmuir models well within the testing range, which means that adsorption occurs on a monolayer surface between Cu(II) and the adsorption sites. The intraparticle diffusion model and various thermodynamic parameters demonstrated that Cu(II) was adsorbed on GFA + KH550 mainly via external surface diffusion and that the process was both endothermic and spontaneous. Recycling experiments show that GFA + KH550 has a satisfactory recyclability, and the way of direct recovery by magnets exhibits good magnetic induction. GFA + KH550 was applied in lake water and artificial seawater samples, and exhibited better removal of copper than that in DI water under the same environmental conditions for the existence of macromolecular organic matter. Furthermore, the adsorption capacity of copper ions was not relative to the salinity of water. The application of GFA + KH550 demonstrated the potential for application in water treatment procedures.

Received 11th July 2021
Accepted 22nd October 2021

DOI: 10.1039/d1ra05160a
rsc.li/rsc-advances

1. Introduction

Heavy metal pollution in water is a worldwide environmental issue and wastewater treatment presents a crucial measure for the mitigation of heavy metal contamination.¹ Since heavy metals are non-degradable and toxic, their removal from water through the development of safe biomaterials is continuing to attract a great deal of attention.² Various methods and techniques, such as chemical precipitation,³ redox,⁴ ion exchange,⁵ flocculation,⁶ adsorption, membrane filtration, electrodialysis, and photocatalysis^{7,8} have been developed to remove copper

(Cu(II)) from wastewater. Here, the adsorption method is regarded as the most promising for Cu(II) removal, largely because of its operational simplicity, cost-effectiveness, and the possibility of regenerating the adsorbents.⁹ However, the recycling operation of current traditional adsorbents is difficult and applied in removing heavy metal from lakes and seawater.¹⁰ Therefore, a new and efficient method needs to be developed to improve adsorption performance in recycling and application in the actual environment. At the same time, magnetic materials for adsorption of heavy metals are commonly used for easily recycling.^{11,12}

In fact, copper is known to pose a risk to aquatic ecosystems since it is generated by numerous industries and is toxic to the environment.¹³ Furthermore, although trace copper ions do not affect normal body functioning, an excessive intake of copper can lead to adverse effects on the immune system.¹⁴ Since copper contaminants are mainly discharged through vessel hull cleaning and maintenance processes,¹⁵ Cu element oxidizes to the more toxic Cu(II) in highly saline water, which leads to intracellular ion imbalance and the inhibition of the enzymatic activity of carbonic anhydrase following excessive intake.¹⁶ The risk of Cu exposure

^aSchool of Chemistry and Chemical Engineering, Oil & Gas Field Applied Chemistry Key Laboratory of Sichuan Province, Southwest Petroleum University, Chengdu, 610500, China. E-mail: wangshunhui@swpu.edu.cn; heyi@swpu.edu.cn; Tel: +86 28 83037367

^bState Key Laboratory of Oil and Gas Reservoir Geology and Exploitation, Chengdu, Sichuan, 610500, China

^cSouthern California Coastal Water Research Project Authority, Costa Mesa, California, 92626, USA

[†] Electronic supplementary information (ESI) available. See DOI: 10.1039/d1ra05160a



through oyster consumption has also increased because of the copper contamination of seawater.¹⁷ Therefore, it is necessary to develop a suitable and easily treatment that can be applied for the removal of this metal from seawater.

Various carbon-based adsorbents have been developed for this purpose.^{10,18,19} Among them, expanded graphite (EG), a 3D worm-like and interconnected porous structure, has been identified as an excellent adsorbent for the removal of heavy metals from wastewater.^{20–22} EG has high solvent-accessible surface areas, excellent accessibility, and reactive functional groups that can be readily modified. In fact, when doped with magnetic components (*e.g.*, Fe_3O_4 and/or CoFe_2O_4), EG adsorbents can be conveniently isolated from the aqueous phase and subsequently regenerated and reused.^{23,24} However, since these magnetic particles do not readily disperse and adhere to the surface of graphene composites, the adsorbents exhibit short stability and reusability.²⁵ Here, there is a strong likelihood that the immobilization of the Fe_3O_4 offers a solution to this issue. Various methods, including impregnation, co-precipitation, and calcination, have been employed to immobilize the magnetic nanocomposites on adsorbents.²⁶ For example, Fe_3O_4 particles were wrapped in graphene oxide (GO) sheets *via* covalent bonding with $-\text{OH}$ in GO and $-\text{NH}_2$ in $\text{Fe}_3\text{O}_4@\text{SiO}_2-\text{NH}_2$ to produce recyclable magnetic adsorbents for removing $\text{Pb}(\text{II})$,²⁷ whereas a magnetic Fe_3O_4 -encapsulated $\text{C}_3\text{N}_3\text{S}_3$ polymer/rGO nanocomposite was synthesized and evaluated for the effective adsorption of $\text{Pb}(\text{II})$ and $\text{Hg}(\text{II})$ from aqueous solutions.²⁸ However, these magnetic composites do not contain sufficient functional groups for adsorption.

PDA coatings are generally produced *via* the self-polymerization of dopamine on the surfaces of different materials. This procedure mimics the adhesive proteins secreted by mussels for attachment to various materials,²⁹ due to inexpensive bio-inspired coatings utilized for the efficient adsorption of transition metal ions such as $\text{Cu}(\text{II})$, $\text{Pb}(\text{II})$, $\text{Ni}(\text{II})$, and $\text{Zn}(\text{II})$ from wastewater^{30–32} as well as oil–water separation/modification and biomedical treatment without the generation of secondary pollutants.^{33–36} Elsewhere, PDA has also been employed to stabilize the Fe_3O_4 attached on cellulose for its resorcinol adsorption from water.³⁷

Meanwhile, silane coupling agents, such as 3-amino propyltriethoxysilane, also known as KH550, has been used to coat $\text{Fe}_3\text{O}_4/\text{rGO}$ composites to increase the electromagnetic wave absorption performance.³⁸ Here, the KH550-modified composites had the capacity to enhance the removal efficiency in relation to various heavy metals, including $\text{Pb}(\text{II})$ and $\text{U}(\text{IV})$.^{39,40} Furthermore, with the addition of KH550, covalent bonding can be formed with a broad range of organic and inorganic surfaces using PDA.⁴¹ However, although PDA and KH550 have been used separately to encapsulate Fe_3O_4 on a number of composites, no report exists in relation to EG/ Fe_3O_4 (EGF) composites encapsulated with both PDA and KH550.

As such, the main aim of the present work was to prepare and characterize a inorganic–organic composite, *i.e.*, EG/ $\text{Fe}_3\text{O}_4/\text{PDA} + \text{KH550}$ (GFA + KH550), for the adsorption and removal of $\text{Cu}(\text{II})$ from water. This composite was prepared on a substrate of EGF functionalized by PDA and KH550. It was

expected that the composite would provide numerous oxygen- and nitrogen-containing functional groups as active sites for binding metal ions *via* electrostatic interaction, coordination, hydrogen bonding, and π – π stacking interactions on both the basal and edge surfaces. To confirm the adsorption performance of the GFA + KH550, two adsorbents, EG/ Fe_3O_4 (EGF) and EG/ $\text{Fe}_3\text{O}_4/\text{PDA}$ (GFA), were also compared. The performance of the composites was reflected in terms of the decrease in the hazard index (HI) of the $\text{Cu}(\text{II})$ in deionized (DI) water, lake water, and artificial seawater. To better understand the adsorption mechanism, the macroscopic adsorption kinetics, isotherms, and thermodynamics of the adsorption were investigated, and the effects of various adsorption parameters, including contact time, initial concentration, pH value, and temperature, were also evaluated. The flowchart for the preparation of the three modified EGFs is shown in Fig. 1.

2. Materials and methods

2.1 Materials

EG powder ($\geq 99\%$) was provided by Daying Juneng Technology and Development Co., Ltd. (Suining, China), dopamine hydrochloride and tri(carboxymethyl)aminomethane ($\geq 98\%$) were purchased from Aladdin Industrial Corporation (Los Angeles, American), and γ -aminopropyl triethoxysilane ($\text{KH550} \geq 90\%$), ethylene glycol (99.7%), anhydrous ethanol (99.8%), polyethylene glycol 2000 (AR), anhydrous sodium acetate (99%), ferric chloride hexahydrate (98%), standard $\text{Cu}(\text{II})$ solution, hydrochloric acid (AR), sodium hydroxide (98%), and nitric acid (65–68%) were supplied by Chengdu Kelong Chemical Reagent Factory (Chengdu, China). The DI water used in the study was prepared using the molecular purifier produced by Shanghai Moller Scientific Instruments Co., Ltd (Molgy, Shanghai, China; $\text{pH} = 6.5 \pm 0.1$).

2.2 Collection of water samples

The lake water was collected from Mengxi Lake of Southwest Petroleum University ($\text{N} 30^{\circ}49'55''$, $\text{E} 104^{\circ}10'58''$), with the pH of the lake water equal to 7.0 ± 0.1 . Meanwhile, the artificial seawater was prepared by dissolving sea salts sourced from Guangzhou Aquarium Factory, China, in the lake water to achieve a salinity of 2.8% , the water left to stand for around 24 h prior to use. The pH of the artificial seawater was 8.0 ± 0.05 . The dissolved organic carbon (DOC) concentration ($2.62 \pm 0.019 \text{ mg L}^{-1}$) in the lake water was quantified using Shimadzu's (Japan) Total Organic Carbon Analyzer (TOC-L) following filtration using a $0.45 \mu\text{m}$ cellulose membrane.

2.3 Preparation of polydopamine and KH550-modified EG materials

2.3.1 Preparation of magnetic expanded graphite EG/ Fe_3O_4 (EGF). Samples of EG powder (1.5 g) and $\text{FeCl}_3 \cdot 6\text{H}_2\text{O}$ (1.5 g) were dispersed and dissolved in ethylene glycol (40 mL) *via* sonication at 25°C for 0.5 h. After adding polyethylene glycol 2000 (1.0 g) and anhydrous sodium acetate (3.6 g), the mixture was stirred at 60°C for 1 h before being transferred to a 100 mL



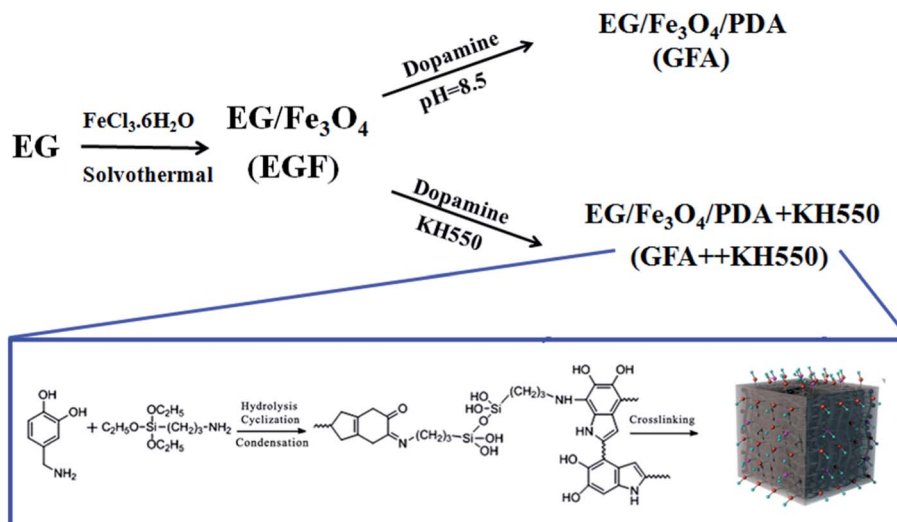


Fig. 1 Synthesis of the PDA- and KH550-modified functional-group-modified rGO composites.

Teflon-lined autoclave and heated at $200\text{ }^\circ\text{C}$ for 12 h. After cooling, the mixture was centrifuged, and the final product was obtained through discarding the supernatant and washing the product using DI water ($\times 3$) and ethanol ($\times 3$). The EGF was then dried in a vacuum oven at $60\text{ }^\circ\text{C}$ for 24 h.

2.3.2 Preparation of composite $\text{EG/Fe}_3\text{O}_4/\text{PDA}$ (GFA). A 200 mg sample of the EGF was dispersed in DI water (50 mL) via sonication for 0.5 h. Following the addition of tris(carboxymethyl)aminomethane (60 mg) at 1.2 g L^{-1} , the pH of the mixture was adjusted to 8.5 before the mixture was agitated for

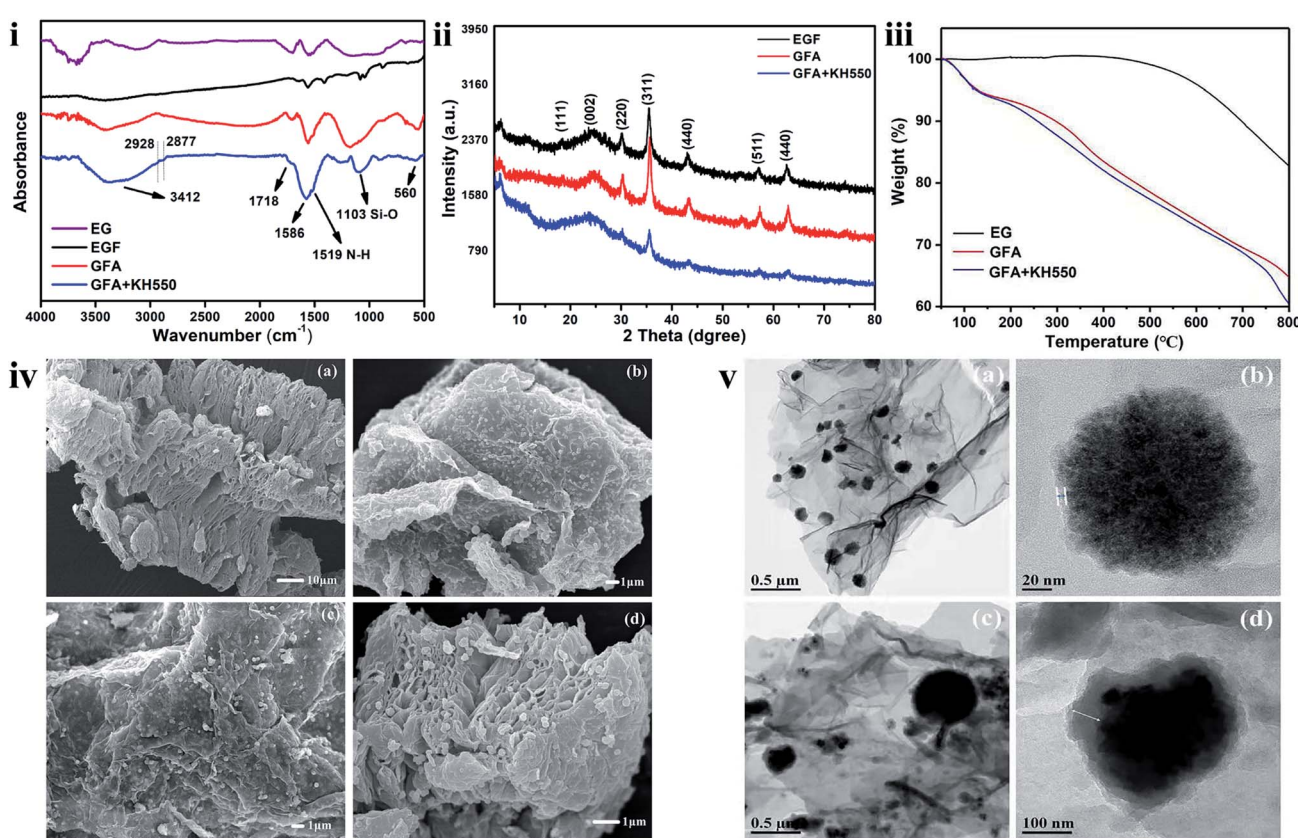


Fig. 2 (i) ATR-FTIR spectra, (ii) XRD pattern, (iii) TGA curve, and (iv) SEM images of (a) EG, (b) EGF, (c) GFA, and (d) GFA + KH550, and (v) TEM images of (a and b) GFA and (c and d) GFA + KH550.



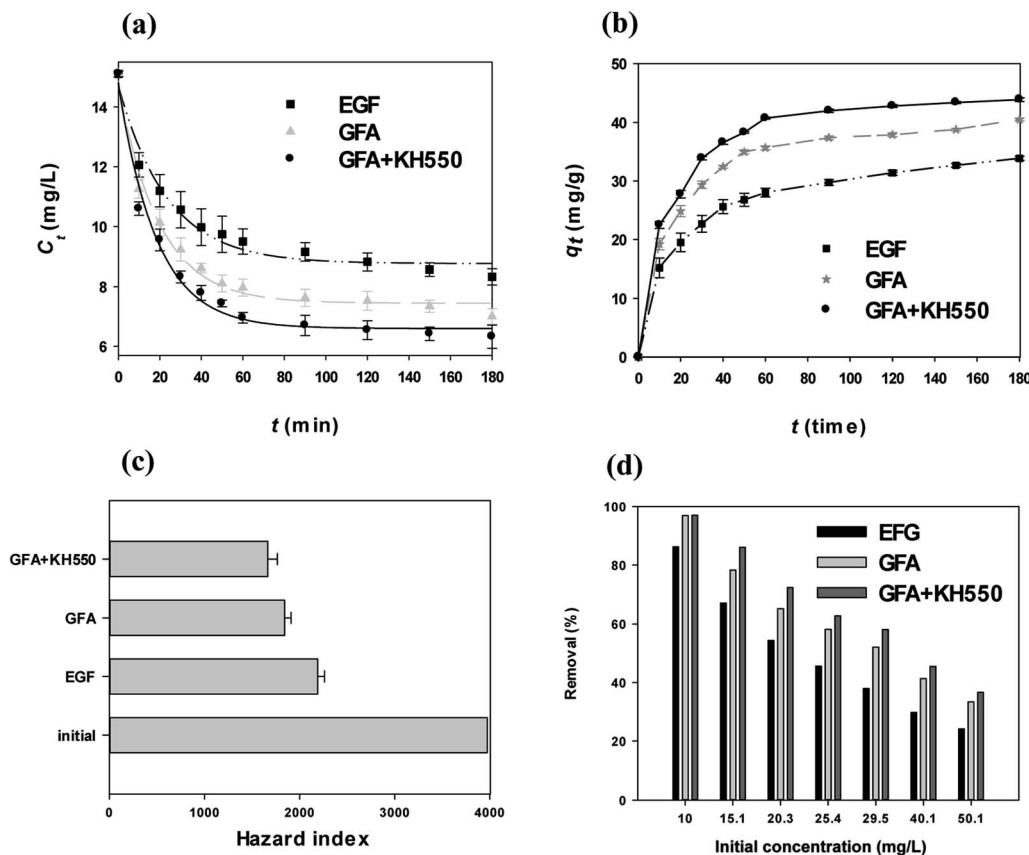


Fig. 3 (a) Cu(II) aqueous concentration vs. adsorption time of the four composites (EGF, GFA, EGF + KH550, and GFA + KH550), (b) concentration of Cu(II) adsorbed on three composites (EGF, GFA, and GFA + KH550) vs. adsorption time, (c) the HI for non-carcinogenic health effects of Cu(II) on adults before and after treatment using three composites (EGF, GFA, and GFA + KH550), and (d) Cu(II) adsorption on the GFA + KH550 with different initial concentrations.

0.5 h. Then, 100 mg of dopamine (2 g L⁻¹) was added to the mixture, the mixture vigorously stirred for 24 h. The GFA was obtained through following the same protocols of centrifugation, washing, and drying as described above.

2.3.3 Preparation of composite EG/Fe₃O₄/PDA + KH550 (GFA + KH550). A 200 mg sample of the EGF was dispersed in DI water (50 mL) under ultrasonic conditions for 0.5 h. Following the addition of tri(carboxymethyl)aminomethane (60 mg) at 1.2 g L⁻¹, the pH of the mixture was adjusted to 8.5 before being agitated for 0.5 h. Then, dopamine (100 mg) was added to the mixture, which was subsequently left for 4 h until the dispersion was complete. The silane coupling agent, KH550 (10 μ L), was then added to the mixture, the mixture vigorously stirred for 24 h. The GFA + KH550 was obtained following the same protocols of centrifugation, washing, and drying as described above.

2.3.4 Characterization. The synthesized composites were characterized using the following techniques: (1) Attenuated Total Reflection-Fourier Transform Infrared Spectroscopy (ATR-FTIR, 4000–500 cm⁻¹, Bruker TENSOR27, German); (2) X-ray Diffraction Analysis (XRD, PANalytical, the Netherlands) using the X'Pert Pro diffractometer with a Cu K α radiation source (scanning amplitude = 5°–80°, scanning rate = 2° min⁻¹); (3) Thermogravimetric Analysis (TGA, TG209F1, Netzsch,

Germany), performed under a N₂ atmosphere in the range of 50–800 °C; (4) X-ray Photoelectron Spectroscopy (XPS, KRATOS, XSAM800, Britain), performed using an EscaLab 250 Xi X-ray photon-electron spectrometer with monochromatic Al K α X-rays adopted as the excitation source and the C 1s peak used to check the energy scale; (5) Scanning Electron Microscopy (SEM); and (6) Transmission Electron Microscopy (TEM). The surface morphology and structure of the materials were observed *via* SEM (JSM-7500 F, JEOL, Tokyo, Japan) after being coated with 10 nm-thick Aurum, and subsequently *via* TEM (Tecnai G2F20, USA).

2.4 Evaluation of performance of the composite materials for removing Cu(II) in aqueous solutions

2.4.1 Comparison of the adsorbents. The adsorptive capacities of the adsorbents (EGF, GFA, and GFA + KH550) were evaluated by recording and comparing the Cu(II) concentrations in a batch sorption experiment using spiked DI water conducted at 25 °C \pm 1 °C. The DI water was spiked with a standard Cu(II) solution to a Cu concentration of 15 mg L⁻¹. After spiking and adjusting the pH value, the solution was thoroughly homogenized for 1 h using a stirrer (IKA C-MAG HS 7 control, German). The adsorbent (10 mg, 0.2 g L⁻¹) was then added to the 50 mL



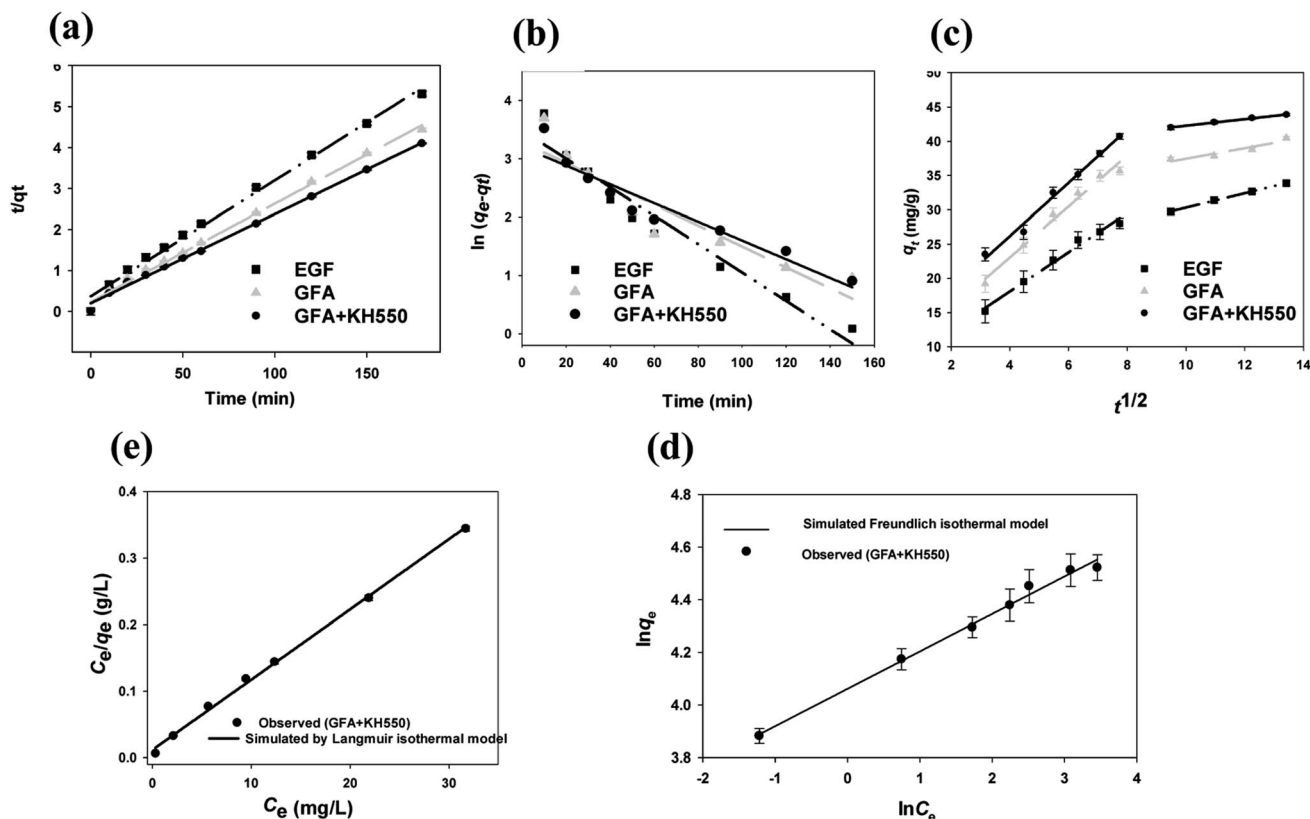


Fig. 4 (a) Pseudo-second-order model fitting curves, (b) pseudo-first-order model fitting curves, (c) intraparticle diffusion model fitting curves (GFA + KH550 composites: 0.2 g L^{-1} , pH = 7, 25°C , initial concentration of Cu(II) = $15.1 \pm 0.1 \text{ mg L}^{-1}$), (d) Langmuir isothermal fitting model, and (e) Freundlich isothermal fitting model.

Cu(II) solution. Triplicates of the mixture were sonicated for 30 s prior to being placed in a water bath with a constant temperature ($25^\circ\text{C} \pm 1^\circ\text{C}$), where they were shaken for 180 min. The Cu(II) concentrations were measured in the water sub-samples that were taken at 5, 20, 30, 40, 50, 60, 90, 120, 150, and 180 min.

2.4.2 Optimization of the adsorption conditions. After the best adsorbent was identified, *i.e.*, GFA + KH550, a series of experiments was conducted to optimize the adsorption conditions while altering one parameter at a time, which included pH (2, 4, 6, 7, 9, and 11, all at $25^\circ\text{C} \pm 1^\circ\text{C}$), temperature (25°C , 35°C , 45°C , and 55°C , all at $\text{pH} = 7.0 \pm 0.1$), and initial concentrations ($10, 15, 20, 25, 30, 40$, and 50 mg L^{-1} , all at $45^\circ\text{C} \pm 1^\circ\text{C}$ and $\text{pH} = 7.0 \pm 0.1$).

2.4.3 Application of the GFA + KH550 in the lake water sample and the artificial seawater sample. The adsorptive capacities of the GFA + KH550 were used in the lake water and the artificial seawater samples spiked with Cu(II), while it was also used in the spiked DI water sample as a control. The three types of water sample were doped with standard Cu(II) to a concentration of 10 mg L^{-1} before being stirred for 1 h. All the adsorption experiments were conducted in triplicate at $45^\circ\text{C} \pm 1^\circ\text{C}$ for 180 min.

2.4.4 Regeneration tests. To assess the reusability of the GFA + KH550 in the DI water and the lake water sample, 10 mg

of the GFA + KH550 was added to a 50 mL Cu(II) (15 mg L^{-1}) solution. The adsorption experiments were repeated for three cycles at $45.0^\circ\text{C} \pm 0.5^\circ\text{C}$ and $\text{pH} = 7.0 \pm 0.1$ for 180 min per cycle. At the end of each cycle, the adsorbent was regenerated *via* the application of an external magnetic field and through washing with 50 mL of HNO_3 solution (0.1 mol L^{-1}) and 50 mL of anhydrous ethanol followed by drying at 60°C for 24 h. The Cu(II) concentration was measured after 5, 10, and 20 cycles. Concurrently, the adsorption experiments were conducted using the control water, with the sampling time intervals the same as those used for the spiked water. The regeneration efficiency was expressed as a percentage, which was calculated by dividing the adsorption capacity following regeneration by the adsorption capacity before regeneration.

The triplicate water samples were filtered using $0.45 \mu\text{m}$ nylon-membrane syringe filters, the filtrates kept in 2% HNO_3 before the Cu(II) concentrations were measured *via* inductively coupled plasma spectrometer-optical emission spectrometry (Agilent ICP-OES 730, USA).

2.5 Data analysis

The removal of Cu(II) from the aqueous solution by the adsorbents can be described in terms of the first-order kinetic model:

$$C_t = b + a \times e^{-\lambda t} \quad (1)$$



Table 1 Kinetic parameters for the pseudo-first-order kinetic model, the pseudo-second-order kinetic model, and the intraparticle diffusion model of Cu(II) adsorption on the GFA + KH550 (0.2 g L⁻¹, pH = 7, 25 ± 1 °C, initial concentration of Cu(II) = 15 mg L⁻¹)

Pseudo-first-order kinetic model	q_{e1} (mg g ⁻¹)	$q_{e,exp}$ (mg g ⁻¹)	k_1 (min ⁻¹)	R^2
EGF	24.6	33.9	0.0140	0.9108
GFA	26.7	40.5	0.0145	0.8678
GFA + KH550	34.7	43.9	0.0247	0.9469

Pseudo-second-order kinetic model	q_{e2} (mg g ⁻¹)	$q_{e,exp}$ (mg g ⁻¹)	k_2 (mg g ⁻¹ min ⁻¹)	R^2
EGF	35.3	33.9	0.0021	0.9927
GFA	41.7	40.5	0.0024	0.9957
GFA + KH550	46.9	43.9	0.0024	0.9970

Intraparticle diffusion model	C_1	k_{i1}	R_1^2
EGF	6.67 ± 1.04	2.85 ± 0.18	0.9850
GFA	8.17 ± 1.48	3.72 ± 0.25	0.9821
GFA + KH550	10.6 ± 1.2	3.89 ± 0.20	0.9897

C_2	k_{i2}	R_2^2	
EGF	19.9 ± 0.3	1.04 ± 0.02	0.9991
GFA	29.7 ± 2.0	0.77 ± 0.17	0.9097
GFA + KH550	37.5 ± 0.2	0.48 ± 0.02	0.9963

Pseudo-first-order kinetic model	q_{e1} (mg g ⁻¹)	$q_{e,exp}$ (mg g ⁻¹)	k_1 (min ⁻¹) (see ESI)	R^2
EGF	24.6	33.9	0.0140	0.9108
GFA	26.7	40.5	0.0145	0.8678
GFA + KH550	34.7	43.9	0.0247	0.9469

Pseudo-second-order kinetic model	q_{e2} (mg g ⁻¹)	$q_{e,exp}$ (mg g ⁻¹)	k_2 (mg g ⁻¹ min ⁻¹)	R^2
EGF	35.3	33.9	0.0021	0.9927
GFA	41.7	40.5	0.0024	0.9957
GFA + KH550	46.9	43.9	0.0024	0.9970

Intraparticle diffusion model	C_1	k_{i1}	R_1^2
EGF	6.67 ± 1.04	2.85 ± 0.18	0.9850
GFA	8.17 ± 1.48	3.72 ± 0.25	0.9821
GFA + KH550	10.6 ± 1.2	3.89 ± 0.20	0.9897

C_2	k_{i2}	R_2^2	
EGF	19.9 ± 0.3	1.04 ± 0.02	0.9991
GFA	29.7 ± 2.0	0.77 ± 0.17	0.9097
GFA + KH550	37.5 ± 0.2	0.48 ± 0.02	0.9963

where C_t is Cu(II) concentration at time t (min) and λ (min⁻¹) is the removal rate constant. The initial concentration C_0 (mg L⁻¹) is equal to $(a + b)$ initial.^{42,43}

The adsorption capacity of the adsorbents (q_t , mg g⁻¹) versus the time was calculated according to the corresponding concentration of Cu(II), as described by eqn (2)

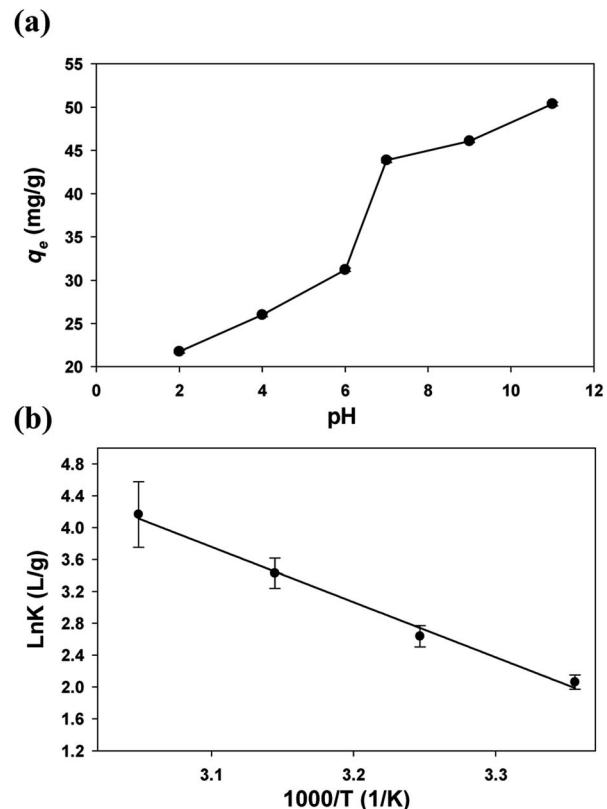


Fig. 5 (a) Effect of pH on the Cu(II) adsorption on the GFA + KH550 and (b) thermodynamic parameters for the adsorption of Cu(II) on the GFA + KH550.

Table 2 The Cu(II) adsorption thermodynamic parameters for the GFA + KH550

Thermodynamic parameters				
T (K)	$\ln K$ (L g ⁻¹)	ΔG^θ (J mol ⁻¹)	ΔS^θ (J [mol K] ⁻¹)	ΔH^θ (J mol ⁻¹)
298	1.94 ± 0.19	-4799 ± 143	70.8 ± 5.0	16 295 ± 1579
308	2.64 ± 0.13	-5488 ± 198		
318	3.43 ± 0.19	-6369 ± 159		
328	4.16 ± 0.41	-6859 ± 169		

$$q_t = \frac{C_0 - C_t}{m_{\text{adsorbent}}} \times V \quad (2)$$

where C_0 (mg L⁻¹) is Cu(II) concentration at the beginning of adsorption (t_0), V (L) is the volume of the aqueous solution, and $m_{\text{adsorbent}}$ (g) is the mass of the adsorbent. The adsorption capacity at equilibrium (q_e , mg g⁻¹) was calculated using eqn (2) with the equilibrium concentration C_e (mg L⁻¹) instead of the C_t .

The removal of Cu(II) from the aqueous solution was assessed using the HI in terms of estimating the possible toxic effects on humans in health risk assessments. The HI was calculated using the following equation.^{44,45}



Table 3 The maximum adsorption capacity (Q_{\max}) of different carbon-based material

Adsorbent	Q_{\max} (mg g ⁻¹)	References
Multi-walled carbon nanotube-decorated Fe_3O_4 ($\text{Fe}_3\text{O}_4/\text{MWCNTs-COOH}$)	10.45	(Temnuch <i>et al.</i> 2020)
Sodium dodecyl sulfate-coated Fe_3O_4 nanoparticles (SDS- Fe_3O_4 NPs)	24.2	(Adeli <i>et al.</i> 2017)
Oxidized sugarcane bagasse (SBox)	36.5	(Rodrigues <i>et al.</i> 2020)
Oxidized cellulose (Cox)	76.8	(Rodrigues <i>et al.</i> 2020)
GO/ Fe_3O_4	18.3–25.6	(Li <i>et al.</i> 2020)
GFA + KH550	94.3	This work

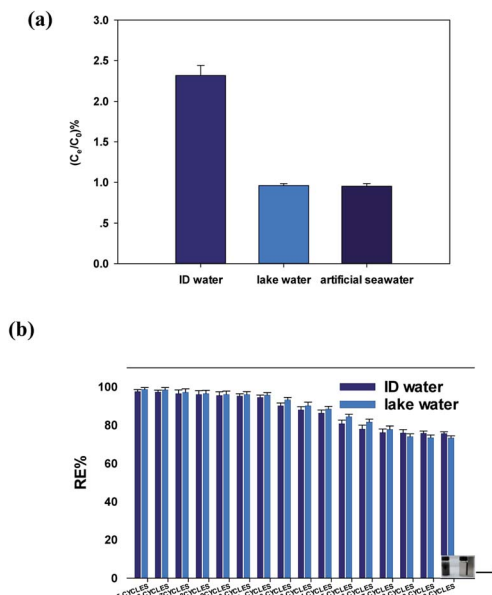


Fig. 6 (a) Adsorption efficiencies of the GFA + KH550 in the spiked lake water, artificial seawater, and DI water samples; (b) regeneration efficiency (RE) of the GFA + KH550 in the spiked DI water and lake water samples.

$$\text{HI} = \frac{\text{CDI}}{\text{RfD}} \quad (3)$$

where RfD (the reference dose for Cu, 0.038 mg per kg per day)⁴⁶ is a numerical estimate of the daily oral exposure to the human population (including sensitive subgroups such as children) that is unlikely to cause harmful effects during a lifetime, and CDI (mg per kg per day) is the chronic daily intake. The CDI was calculated as follows.⁴⁴

$$\text{CDI} = \frac{C_{\text{water}} \times \text{WI} \times \text{ED} \times \text{EF}}{\text{BW} \times \text{AT}} \quad (4)$$

where C_{water} is Cu(II) concentration in the water (mg L⁻¹), WI is water intake rate (= 2 L per day), ED is the exposure duration (=30 years), EF is the exposure frequency (=350 days per year), BW is the body weight of an adult (=70 kg), and AT is the average time of exposure, which is 30 years for non-carcinogenic compounds or 70 years (lifetime) for carcinogenic compounds.

The adsorption kinetics was characterized using pseudo-first-order and pseudo-second-order kinetic models.⁴⁷ The pseudo-second-order kinetic model is as follows:

$$\frac{t}{q_t} = \frac{1}{k_2 q_e^2} + \frac{t}{q_e} \quad (5)$$

whereas the pseudo-first-order model is as follows:

$$\ln(q_e - q_t) = \ln q_e - k_1 t \quad (6)$$

where k_2 (mg g⁻¹ min⁻¹) is the adsorption rate constant of the second-order rate model and k_1 (min⁻¹) is the adsorption rate constant of the first-order rate model.

To describe the diffusion-controlled processes in the adsorption stages, the intraparticle diffusion model was used as follows:

$$q_t = k_{\text{intra}}(t)^{1/2} + C \quad (7)$$

where k_{intra} (mg g⁻¹ min^{-0.5}) is the intraparticle diffusion rate constant and C (mg g⁻¹) is a constant related to the thickness of the boundary layer.⁴⁷

Meanwhile, the Langmuir and Freundlich models were used to determine the maximum adsorption capacity of the adsorbent.^{48,49} The Langmuir and Freundlich models are as follows:

$$\frac{C_e}{q_e} = \frac{1}{K_L q_{\max}} + \frac{C_e}{q_{\max}} \quad (8)$$

$$\ln q_e = \ln K_F + \frac{1}{n} \ln C_e \quad (9)$$

where K_L (L mg⁻¹) is the Langmuir constant and q_{\max} (mg g⁻¹) represents the maximum adsorption capacity of the adsorbent. K_F is Freundlich constant representing adsorption capacity.

The thermodynamic parameters were used to determine the spontaneity, disorder, and endothermic or exothermic properties of the adsorption process. The standard enthalpy variable (H^θ), standard entropy variable (S^θ), and standard Gibbs free energy variable (G^θ) relative to the adsorption process were calculated using the following equations:

$$\ln K = -\frac{\Delta H^\theta}{RT} + \frac{\Delta S^\theta}{R} \quad (10)$$

$$\Delta G^\theta = -RT \ln K \quad (11)$$

where R is the gas constant 8.314 J mol⁻¹ K⁻¹ and T (K) is the temperature in kelvin; here, K (= q_e/C_e , L g⁻¹) is the equilibrium constant at the different temperatures.

3. Results and discussion

3.1 Preparation strategy

The synthesis of the EGF, GFA, and GFA + KH550 is illustrated in Fig. 1. To synthesize the EGF, a co-precipitation method was used to load Fe_3O_4 particles on the EG. The Fe_3O_4 particles were immobilized on the EG *in situ* using $\text{FeCl}_3 \cdot 6\text{H}_2\text{O}$ *via* solvothermal reaction. The EGF was further coated with PDA, and PDA/KH550 to form GFA, and GFA + KH550, respectively.

It is worth noting that the bio-inspired modification of the EGF using the PDA and KH550 produced a large amount of hydroxyl and amino groups, which enhanced the hydrophilicity and adsorption performance. Dopamine was easily self-assembled and adhered to the surface of the material under mild conditions, which provided further hydrophilic functional groups *via* surface modification.⁵⁰ The adherence of the KH550 to the composite also improved its hydrophilicity. The PDA- and KH550-modified composites could also be applied to other wastewater treatments owing to their ability to enhance the adsorption performance of methylene blue, and the separation of oil-in-water emulsion and dye with ultrahigh efficiency.⁵¹⁻⁵³

3.2 Characterization of the composites

The materials were characterized *via* FTIR, XRD, TGA, XPS, SEM, and TEM analyses to evaluate the synthesis performance and structural features. The characteristic stretching frequencies of the EG, EGF, GFA, and GFA + KH550 in the FTIR spectra are shown in Fig. 2i. In each of these spectra, a broad absorption peak at around 3412 cm^{-1} was observed, which matched the characteristic peaks of $-\text{OH}$ groups. With the addition of dopamine and KH550, the peak intensity of the GFA, and GFA + KH550 was significantly stronger than that of the EG and EGF, indicating that the dopamine and KH550 brought more $-\text{OH}$ to form the GFA, and GFA + KH550. The bend vibration of $-\text{NH}$ was observed at 1519 cm^{-1} in the GFA, and GFA + KH550 spectra. The absorption peaks observed at 2877 and 2928 cm^{-1} corresponded to the symmetric and non-symmetric stretching vibration of $-\text{CH}_2$ afford by PDA and KH550, whereas the band at 1103 cm^{-1} resulted from the stretching vibration of the Si–O of the KH550. Meanwhile, the two peaks at 1718 and 1586 cm^{-1} were attributed to the characteristic peaks of the $\text{C}=\text{O}$ and $\text{C}=\text{C}$ of the EG. The existence of a strong peak of $\text{C}=\text{C}$ stretching vibration overlapped with the $\text{C}=\text{N}$ peak, and this likely led to the absence of $\text{C}=\text{N}$ bending. Moreover, an absorption band at 560 cm^{-1} was observed, which was ascribed to the peak of Fe–O vibration. These results indicated that the dopamine and KH550 were coated on the EGF sheets and GFA, and GFA + KH550 were successfully synthesized.

The XRD patterns of EGF and the surface-modified EGF composites, including GFA, EGF + KH550, and GFA + KH550, are shown in Fig. 2ii. In all of the patterns, the diffraction peak at $2\theta = 24.4^\circ$ was attributed to the graphitic structure of EG and the modified EGF. Six characteristic peaks were observed for all the samples at $2\theta = 18.3^\circ, 30.1^\circ, 35.5^\circ, 43.0^\circ, 57.1^\circ$, and 62.7° , which were attributed to the crystal planes of cubic spinel Fe_3O_4 of (111), (220), (311), (440), (511), and (440), respectively.

Following the surface functionalization, the intensity of the GFA + KH550 diffraction peaks became weak owing to the coverage of the PDA and KH550 on the surface of the EGF. These results demonstrated that Fe_3O_4 nanoparticles were loaded on the EG. Moreover, the diffraction peak positions of the GFA + KH550 were consistent with those of the EGF, indicating the unchanged crystalline phase of Fe_3O_4 following the reaction.

Meanwhile, TGA was used to examine the modification content of the dopamine on the EG (Fig. 2iii). The weight of the pure EG did not change significantly up to $450\text{ }^\circ\text{C}$, indicating the high thermal stability of this material. With the increase in temperature, the EG functional groups gradually decomposed, whereas the carbon structure remained at the end of the reaction, with only around 17.0 wt% of oxygen functional groups left on the EG. The GFA and GFA + KH550 presented distinct degradation behavior compared with the EG. When the temperature was higher than $100\text{ }^\circ\text{C}$, the GFA and GFA + KH550 were clearly decomposed, with the final mass losses around 35.3 and 39.5 wt% following heating from $50\text{ }^\circ\text{C}$ to $800\text{ }^\circ\text{C}$. The reason for the loss in the weight of the GFA related to the decomposition and detachment of the self-polymerized dopamine and Fe_3O_4 particles on the surface of the EG upon heating. Consequently, only 18.3 wt% of PDA and Fe_3O_4 remained on the EG. Similarly, on the EGF + KH550, the remaining amount of grafted KH550 following heating was around 4.2%.

The SEM images are presented in Fig. 2iv. The gap between the EG layers increased significantly following high-temperature treatment owing to the formation of a honeycomb-like porous structure. The surfaces of the EGF became rougher, and the distances between EG lamellae also increased after coating with the PDA + KH550 (Fig. 2ivd). The Fe_3O_4 nanoparticles generated in the subsequent solvothermal reaction process were uniformly loaded on the surfaces of the three materials. The binding between the Fe_3O_4 nanoparticles and the EG lamellae was assumed to be highly stable since the attachment of Fe_3O_4 nanoparticles did not diminish following the modification with the dopamine and KH550.

The TEM images further confirmed the successful loading of Fe_3O_4 nanoparticles on the EG substrate (Fig. 2v). Here, a thin coating layer on the surface of the Fe_3O_4 nanoparticles was observed (Fig. 2vb), indicating that the degree of self-polymerization of the dopamine on the surface of EGF was not high. However, after adding a small amount of KH550, a thicker organic layer formed because of the co-grafting of the dopamine and KH550 (Fig. 2vd), which indicated that the degree of copolymerization of the dopamine and KH550 was higher than that of the dopamine alone.

To further investigate the composition and elemental chemical states of the composite materials, XPS was employed. The same components, *i.e.*, C 1s (284.0 eV), O 1s (533.3 eV), Fe 2p₁ (725.0 eV), and Fe 2p₃ (711.9 eV), were appeared in the wide-scan spectra of the EGF (Fig. S1a†).^{11,12,52} The C 1s core-level spectrum of the EGF was divided into four peak components: C–C (284.6 eV), C–O (286.6 eV), C=O (288.4 eV), and O=C=O (290.3 eV) (Fig. S1b†).¹¹ In terms of the GFA (Fig. S1c and d†), there was another characteristic peak at 401.3 eV, which was attributed to N 1s and the peaks of C–N at 285.4 eV in the



attendant C 1s core-level spectrum.¹¹ The Fe 2p₁ and Fe 2p₃ peaks of the GFA were clearly weaker than the peak of the EGF. Meanwhile, the peaks of N 1s, C-Si (282.4 eV)⁵² and C-N, as well as a Fe 2p intensity reduction, were also observed in the total spectrum and the C 1s spectrum of the GFA + KH550 (Fig. S1e and f†). The peaks at 168.35 and 89.76 eV corresponded to the Si 2s and Si 2p of the KH550 on the GFA + KH550.¹² The presence of a C=N bond at 286.48 eV confirmed that there was a cross-linking reaction between the dopamine and the KH550, indicating that the two components had been successfully co-grafted (Fig. S1e†).⁵¹ The C 1s peaks of the EGF indicated that the EG contained numerous oxygen-bearing functional groups. Even after the loading of Fe₃O₄ particles, abundant active sites still remained (Fig. S1d†). The N 1s and C-N peaks shown in Fig. S1e and f† confirmed that the dopamine had successfully self-polymerized on the surface of the EGF (Fig. S1a, c and e†).

3.3 Capability of removing Cu(II) from water and regeneration assessment

The removal of Cu(II) by the three composites, *i.e.*, the EGF, GFA, and GFA + KH550, was observed; however, the extent of the removal differed among them (Fig. 3a). The Cu(II) concentrations (C_t) of the water treated with the EGF were significantly different from those in the water treated with the GFA and GFA + KH550, starting from 40 min until the end of the experiment at 180 min (one-way ANOVA, $p < 0.05$). The recorded C_t s values were 8.33 ± 0.27 (EGF), 7.00 ± 0.26 (GFA), and 6.33 ± 0.39 mg L⁻¹ (GFA + KH550), and the remove rate of copper ions the three adsorbents are 86.2%, 96.9%, and 97.0%. The GFA + KH550 demonstrated the highest efficiency in terms of Cu(II) removal. The C_t versus time (eqn (1)) fitted well ($R^2 = 0.9678 \sim 0.9858$) with the first-order kinetic model (eqn (12)–(14)):

$$C_t(\text{EGF}) = (8.76 \pm 0.18) + (5.99 \pm 0.35) \times e^{-(0.0425 \pm 0.0054) \times t} \quad (12)$$

$$C_t(\text{GFA}) = (7.45 \pm 0.15) + (7.39 \pm 0.32) \times e^{-(0.0514 \pm 0.0048) \times t} \quad (13)$$

$$C_t(\text{GFA+KH550}) = (6.59 \pm 0.22) + (8.08 \pm 0.47) \times e^{-(0.0508 \pm 0.0064) \times t} \quad (14)$$

The adsorption capacity (q_t , eqn (2)) of all three selected composites increased with the increase in adsorption time (Fig. 3b), with the q_t values approaching a plateau after 120 min. Meanwhile, the equilibrium adsorption capacities (q_e , eqn (2)) were 33.9 ± 0.4 (EGF), 40.5 ± 0.2 (GFA), and 43.9 ± 0.3 mg g⁻¹ (GFA + KH550). The q_e value of the GFA + KH550 was clearly the highest among the three composites. The PDA was combined with the KH550 *via* condensation to provide more adsorption-active sites.^{12,54} The IR, SEM, and TEM results were in line with these findings (Fig. 2).⁵²

The HI was used to further illustrate the Cu(II)-removal efficiency. For non-carcinogenic risk assessment, with the initial Cu(II) concentration of 15.1 ± 0.1 mg L⁻¹, the HI value of Cu for adults was 3974 ± 26 , as calculated using eqn (3) and (4). The HI values shifted to 2191 ± 71 (EGF), 1843 ± 68 (GFA), and 1664 ± 102 (GFA + KH550) following the adsorption experiments,

which lasted for 180 min. Compared with the initial Cu(II) concentration, the HI risk of the Cu(II)-spiked water treated using the GFA + KH550 declined more than twofold, with the HI reduction = 2310 ± 72 , which was better than that of the EGF (1783 ± 75) and the GFA (2131 ± 105). For the initial concentration from 10 mg L⁻¹ to 50.1 mg L⁻¹, the removal efficiency of GFA + KH550 were 97.0–36.7%, which were the best for Cu(II) among the three adsorbents at the same initial concentration. This confirmed that the GFA + KH550 was the most effective in getting rid of Cu(II) in water (Fig. 3d).

3.4 Adsorption kinetics and adsorption isotherms

The Cu(II) adsorption kinetics of the EGF, GFA, and GFA + KH550 were described well by the pseudo-second-order kinetic model (eqn (5), Fig. 4a). Here, the R^2 values of the three composites were all above 0.99 (Table 1). Meanwhile, the equilibrium adsorption capacity (q_{e2}) values were 35.3 (EGF), 41.7 (GFA), and 46.9 mg g⁻¹ (GFA + KH550), which were very close to the experimental values ($q_{e,\text{exp.}} = 33.9, 40.5$, and 43.9 mg g⁻¹, respectively). In contrast, the R^2 values obtained *via* the pseudo-first-order kinetic model (eqn (6)) ranged from 0.87 to 0.95 (Fig. 4b). The corresponding equilibrium adsorption capacity (q_{e1}) values were 24.6 (EGF), 26.7 (GFA), and 34.7 mg g⁻¹ (GFA + KH550). In line with previous studies, the pseudo-second-order kinetic model adequately described the measured Cu(II) adsorption dynamic behavior.^{54,55}

The adsorption processes of the three materials all exhibited two different stages, as identified by fitting the adsorption data in the intraparticle diffusion model (eqn (7), Fig. 4c). The diffusion rates of the first stage (k_{i1}) were 2.85 ± 0.18 , 3.72 ± 0.25 , and 3.89 ± 0.20 mg g⁻¹ min^{-1/2} for the EGF, GFA and GFA + KH550, respectively, whereas the diffusion rates of the second stage (k_{i2}) were 1.04 ± 0.02 , 0.77 ± 0.17 , and 0.48 ± 0.02 mg g⁻¹ min^{-1/2}, respectively. Meanwhile, the intercept C values of the first stage were 6.67 ± 1.04 (EGF), 8.17 ± 1.48 (GFA), and 10.6 ± 1.2 mg g⁻¹ (GFA + KH550), whereas those of the second stage were 19.9 ± 0.3 (EGF), 29.7 ± 2.0 (GFA), and 37.5 ± 0.2 mg g⁻¹ (GFA + KH550).

The diffusion rate constant of the first stage was much higher than those of the second stage. For example, the k_{i1} of the GFA + KH550 was 8.1 times higher than the k_{i2} . In contrast, the C values of the first stage were smaller than those of the second stage. The C value was related to the thickness of the boundary layer; *i.e.*, the larger the C value, the thicker the boundary layer. Therefore, the C values indicated that the thicknesses of the boundary layer of the GFA + KH550 were the highest among the four materials in both stages, which was in line with the SEM images. Meanwhile, the highest q_{e2} and k_{i1} of the first stage and the smallest k_{i2} of the second stage for the GFA + KH550 suggested that the first stage presented surface diffusion, whereas the second stage presented pore diffusion. The cross-linking between the PDA and the KH550 on the GFA + KH550 accelerated the first stage on the surface diffusion but slowed down the second stage on the pore diffusion.⁵⁶ Therefore, the adsorption process of Cu(II) on the GFA + KH550 was



more significantly influenced by the external surface diffusion than the internal diffusion.

The Langmuir and Freundlich isotherm models are used to investigate the adsorption mechanism of Cu(II) by GFA + KH550 absorbent material respectively. As shown in Fig. 4d and e, the Langmuir isotherm model shows better linear fitting than the Freundlich isotherm model. Here, the maximum adsorption capacity (Q_{\max}) was 94.3 mg g⁻¹, whereas K_L was 0.906 L mg⁻¹, as based on the Langmuir isotherm model, while The K_F was 57.7 L g⁻¹ calculated by eqn (9) based on the Freundlich isotherm. The adsorption data for the GFA + KH550 fitted well with the Langmuir isotherm model (eqn (8), coefficient $R^2 = 0.9980$) within the experimental range while the coefficient R^2 of Freundlich isotherm model was only 0.9743 (Fig. 4d). Accordingly, Langmuir model's coefficient is higher than Freundlich model's, showing that Langmuir isotherm model better describes the adsorption process than Freundlich model. Therefore, a monolayer adsorption occurred on the heterogeneous surface of EG + KH550 towards Cu(II), and the adsorption mechanism was predominantly chemical adsorption.^{57,58} Surprisingly, as shown in Table 3, the Q_{\max} of the GFA + KH550 was higher than those of multi-walled carbon nanotube-decorated Fe₃O₄ (Fe₃O₄/MWCNTs-COOH; 10.45 mg g⁻¹), sodium dodecyl sulfate-coated Fe₃O₄ nanoparticles (SDS-Fe₃O₄ NPs; 24.2 mg g⁻¹), oxidized sugarcane bagasse (SBox; 36.5 mg g⁻¹), and oxidized cellulose (Cox; 76.8 mg g⁻¹),⁵⁹⁻⁶¹ and it was also higher than those (18.3–25.6 mg g⁻¹) of several GO/Fe₃O₄ composites for the adsorption of Cu(II).⁶² This was likely because there were more available adsorption sites on the GFA + KH550 than on the other materials.⁶¹

3.5 The effects of solution pH and temperature on adsorption

The solution pH had a significant impact on the adsorption performance. As shown in Fig. 5a, the q_e of the GFA + KH550 generally increased with the increase in pH value, with the values = 46.1 mg g⁻¹ at pH 9 and 21.7 mg g⁻¹ at pH 2 (eqn (2)). From pH 6 to pH 7, there was a pronounced increase in adsorption capacity. Non-electrostatic and electrostatic interactions are generally the main adsorption mechanisms that emerge on the surface of composite adsorbents.⁶³ With the further increase of pH, Cu²⁺ existed in the form of Cu(OH)₂ in water and was adsorbed by the GFA + KH550 easily.⁶⁴ This correlation between q_e and pH value indicated that the adsorption was related to the interaction of the positive and negative charges on the surface of the adsorbent. The functional groups of the GFA + KH550 are protonated and take on the form of -NH₂⁺ and -OH₂⁺ under acidic conditions. The increase in solution pH leads to more primary amine and hydroxyl groups forming the structure of -NH and -OH, whereas Cu²⁺ and H⁺ always compete to occupy adsorption sites containing O and N.^{12,52} In addition, the surface of the GFA + KH550 is positively charged, which leads to electrostatic repulsion between the electropositive Cu(II) and the sorbent's surface under acidic conditions. Here, the surface gradually becomes negatively charged when increasing the pH, and forces of

attraction enhance the sorption by facilitating the interaction between the metal ions and the active sites.⁶⁵ But the adsorption of Cu(II) was discussed in the form of ions in this study. Therefore, we considered that pH = 7 was the most suitable values for Cu(II) adsorption.

An increase in temperature was favorable to the adsorption. The relationship between thermodynamic equilibrium constant $\ln K$ and 1000/T was depicted by the van't Hoff plot with a high R^2 value (0.9814, Fig. 5b). The ΔH^θ (16 295 ± 1579 J mol⁻¹), ΔS^θ (70.8 ± 5.0 J [mol K]⁻¹), and ΔG^θ values were all calculated (eqn (9) and (10), Table 2). The positive ΔH^θ values indicated that the adsorption presented an endothermic process. Therefore, increasing the temperature of the system would likely favor the adsorption.¹² Meanwhile, the positive ΔS^θ value indicated an increase in randomness at the interface between the solid and the solution. Finally, the ΔG^θ value was negative, implying that the adsorption presented a spontaneous process.⁶⁶

3.6 Application and regeneration of the GFA + KH550 in the field-collected water samples

The adsorption potential of the GFA + KH550 for Cu(II) removal from the DI water, lake water, and artificial seawater samples was further examined. The ratios of Cu(II) equilibrium concentration and initial concentration were 2.32% ± 0.12%, 0.960% ± 0.024%, and 0.952% ± 0.034%, for the DI water, lake water, and artificial seawater samples, respectively (Fig. 6a). Clearly, the ratio of Cu(II) concentration in the DI water was significantly higher than those in the lake water ($p < 0.05$) and artificial water ($p < 0.05$), with the ratios similar for the latter two ($p = 0.76$). Using the same absorbent amount under the same environmental conditions, the adsorption capacity in the lake water and artificial seawater samples was slightly better than that in the DI water. This difference was likely due to the Cu(II) associating with the DOC in the matrix of the field-collected water samples. It has previously been reported that macromolecular organic matters in natural water, such as humic acid and fulvic acid, provide specific adsorption sites that easily form complexes with metal ions in an aqueous system with a pH of 6–8.⁶⁷ Here, although more inorganic ions exist in artificial seawater than in lake water, the adsorption capacity of Cu(II) did not decrease, which indicated that the Cu(II) adsorption was not affected by the salinity.

Meanwhile, regeneration was performed to investigate the adsorption potential of the GFA + KH550 in the DI water and lake water samples over multiple treatment cycles. Here, the regeneration efficiency in the first five cycles was 97.6% ± 0.5% and 98.7% ± 0.5% for the DI water and the lake water, respectively (Fig. 6b), whereas the regeneration efficiencies of the 10th cycle were 97.2% ± 0.5% and 97.0% ± 0.5%, respectively. Since there was no significant difference between the 5th and 10th cycles for the DI water ($p = 0.383$), the GFA + KH550 clearly exhibited good reusability after 10 cycles. However, the regeneration efficiencies of the 20th cycle were 75.7% ± 0.4% and 73.4% ± 0.4% for the DI water and the lake water, respectively, which indicated a clear decrease. This was likely because the Schiff base structure C=N formed by the



condensation of PDA was broken and hydrolyzed by HNO_3 during the regeneration process,^{68,69} with the breaking of the $\text{C}=\text{N}$ bonds leading to the reduction in adsorption sites. Using other regeneration reagents and the protection of the $\text{C}=\text{N}$ bonds should be a focus of future investigations.

4. Conclusions

In this study, we demonstrated that the dual coating of PDA and KH550 significantly improves the adsorption capacity and reusability of EGF. The hybrid inorganic-organic composite, GFA + KH550, was easily prepared *via* solvothermal reaction. Based on the structural characterization, the GFA + KH550 exhibited excellent adsorption for $\text{Cu}(\text{II})$, with its adsorption capacity affected by the time, pH, and temperature. The application of this material could reduce the HI of water contaminated with $\text{Cu}(\text{II})$.

Funding

This work was supported by the National Nature Science Foundation of China (51774245), Open Fund of Oil & Gas Field Applied Chemistry Key Laboratory of Sichuan Province (YQKF202008), the Opening Project of Oil & Gas Field Applied Chemistry Key Laboratory of Sichuan Province (YQKF202008) and Scientific Research Starting Project of Southwest Petroleum University (2019QHZ004).

Author contributions

Shunhui Wang: data curation, writing – original draft, funding acquisition. Wenjian Lao: writing – review & editing, project administration. Yi He: supervision, funding acquisition. Heng Shi: methodology, investigation. Qihang Ye: investigation, validation. Jing Ma: methodology.

Conflicts of interest

The authors have no conflicts of interest.

Acknowledgements

The authors appreciate C. Lao and Z. H. Long for assistance with editing the manuscript. This work is dedicated to the people who are fighting against COVID-19.

References

- 1 S. Wadhawan, A. Jain, J. Nayyar and S. K. Mehta, Role of nanomaterials as adsorbents in heavy metal ion removal from waste water: a review, *J. Water Process. Eng.*, 2020, **33**, 101038.
- 2 Q. Zhang, Q. X. Hou, G. X. Huang and Q. Fan, Removal of heavy metals in aquatic environment by graphene oxide composites: a review, *Environ. Sci. Pollut. Res. Int.*, 2020, **27**(1), 190–209.
- 3 T. A. Kravchenko, L. L. Polyanskiy, V. A. Krysanov, E. S. Zelensky, A. I. Kalinitchev and W. H. Hoell, Chemical precipitation of copper from copper-zinc solutions onto selective sorbents, *Hydrometallurgy*, 2009, **95**(1–2), 141–144.
- 4 L. Xie and Z. Tian, Removing copper ion from seawater with redox method, *Chem. Ind. Eng. Prog.*, 2012, **31**(9), 1899–1902.
- 5 L. Rozhdetsvenska, I. Monzie, S. Chanel, A. Mahmoud and F. Lapicque, Ion exchange-assisted electrodialysis for treatment of dilute copper-containing wastes, *Chem. Ing. Tech.*, 2001, **73**(6), 761.
- 6 Y. G. Yang, Y. L. Yang and X. H. Kang, Removal of copper ion in industrial wastewater by magnetic flocculation experimental research, *Appl. Mech. Mater.*, 2013, **295–298**, 1231–1234.
- 7 L. L. Lin, G. G. Liu and W. Y. Lv, Simultaneous Oxidation of Citric Acid and Reduction of Copper Ion by TiO_2 Photocatalysis, *Adv. Mater. Res.*, 2012, **485**, 253–256.
- 8 S. A. Al-Saydeh, M. H. El-Naas and S. J. Zaidi, Copper removal from industrial wastewater: a comprehensive review, *J. Ind. Eng. Chem.*, 2017, **56**, 35–44.
- 9 W. J. Peng, H. Q. Li, Y. Y. Liu and S. X. Song, A review on heavy metal ions adsorption from water by graphene oxide and its composites, *J. Mol. Liq.*, 2017, **230**, 496–504.
- 10 B. Chen, Q. Ma, C. Tan, T. T. Lim, L. Huang and H. Zhang, Carbon-based sorbents with three-dimensional architectures for water remediation, *Small*, 2015, **11**(27), 3319–3336.
- 11 Y. Q. Zhan, Z. H. Long, X. Y. Wan, J. M. Zhang, S. J. He and Y. He, 3D carbon fiber mats/nano- Fe_3O_4 hybrid material with high electromagnetic shielding performance, *Appl. Surf. Sci.*, 2018, **444**, 710–720.
- 12 X. Y. Wan, Y. Q. Zhan, Z. H. Long, G. Y. Zeng and Y. HE, Core@double-shell structured magnetic halloysite nanotube nano-hybrid as efficient recyclable adsorbent for methylene blue removal, *Chem. Eng. J.*, 2017, **330**, 491–504.
- 13 S. N. Hou, N. Zheng, L. Tang, X. F. Ji, X. F. Ji, Y. Y. Li and X. Y. Hua, Pollution characteristics, sources, and health risk assessment of human exposure to Cu, Zn, Cd and Pb pollution in urban street dust across China between 2009 and 2018, *Environ. Int.*, 2019, **128**, 430–437.
- 14 X. Z. Huang, X. Y. Jiang, M. Sun, S. Dupont, W. Huang, M. H. Hu, Q. Z. Li and Y. J. Wang, Effects of copper on hemocyte parameters in the estuarine oyster *Crassostrea rivularis* under low pH conditions, *Aquat. Toxicol.*, 2018, **203**, 61–68.
- 15 A. P. dos Santos, J. H. H. Seta, V. V. Kuhnen and E. G. Sanches, Antifouling alternatives for aquaculture in tropical waters of the Atlantic Ocean, *Aquac. Rep.*, 2020, **18**, 100477.
- 16 T. M. Lopes, I. F. Barcarolli, C. B. De Oliveira, M. M. De Souza and A. Bianchini, Effect of copper on ion content in isolated mantle cells of the marine clam *Mesodesma mactroides*, *Environ. Toxicol. Chem.*, 2011, **30**, 1582–1585.
- 17 L. F. Wang, X. F. Wang, H. G. Chen, Z. H. Wang and X. P. Jia, Oyster copper levels in the northern South China Sea from 1989 to 2015: spatiotemporal trend detection and human



health implications, *Environ. Sci. Pollut. Res. Int.*, 2020, **27**, 37384–37394.

18 M. Fronczak, Adsorption performance of graphitic carbon nitride-based materials: Current state of the art, *J. Environ. Chem. Eng.*, 2020, **8**, 104411.

19 X. Liu, R. Ma, X. Wang, Y. Ma, Y. Yang, L. Zhuang, S. Zhang, R. Jehan, J. Chen and X. Wang, Graphene oxide-based materials for efficient removal of heavy metal ions from aqueous solution: a review, *Environ. Pollut.*, 2019, **252**, 62–73.

20 Z. L. Hu, L. M. Cai, J. M. Liang, X. T. Guo, W. Li and Z. J. Huang, Green synthesis of expanded graphite/layered double hydroxides nanocomposites and their application in adsorption removal of Cr(VI) from aqueous solution, *J. Clean. Prod.*, 2019, **209**, 1216–1227.

21 Z. Liu, F. Pan, B. Deng, Z. Xiang and W. Lu, Self-assembled MoS₂/3D worm-like expanded graphite hybrids for high-efficiency microwave absorption, *Carbon*, 2021, **174**(6), 59–69.

22 X. Wang, X. Wang, J. Zhao, J. Song, L. Zhou, J. Wang, X. Tong and Y. Chen, An alternative to in situ photocatalytic degradation of microcystin-LR by worm-like N, P co-doped TiO₂/expanded graphite by carbon layer (NPT-EGC) floating composites, *Appl. Catal., B*, 2017, **206**, 479–489.

23 C. Z. Li, Y. H. Dong, J. J. Yang, Y. Y. Li and C. C. Huang, Modified nano-graphite/Fe₃O₄ composite as efficient adsorbent for the removal of methyl violet from aqueous solution, *J. Mol. Liq.*, 2014, **196**, 348–356.

24 M. J. Xu, J. Li, Y. Yan, X. G. Zhao, J. F. Yan, Y. H. Zhang, B. Lai, X. Chen and L. P. Song, Catalytic degradation of sulfamethoxazole through peroxymonosulfate activated with expanded graphite loaded CoFe₂O₄ particles, *Chem. Eng. J.*, 2019, **369**, 403–413.

25 X. F. Shu, H. D. Ren, Y. Jiang, J. Zhou, Y. Q. Wang, Y. F. Wang, Y. Liu and W. C. Oh, Enhanced electromagnetic wave absorption performance of silane coupling agent KH550@Fe₃O₄ hollow nanospheres/graphene composites, *J. Mater. Chem. C*, 2020, **8**, 2913–2926.

26 A. Abu-Nada, G. McKay and A. Abdala, Recent Advances in Applications of Hybrid Graphene Materials for Metals Removal from Wastewater, *Nanomaterials*, 2020, **10**, 595.

27 Z. L. Hu, S. L. Qin, Z. Huang, Y. R. Zhu, L. J. Xi and Z. H. Li, Recyclable graphene oxide-covalently encapsulated magnetic composite for highly efficient Pb (II) removal, *J. Environ. Chem. Eng.*, 2017, **5**, 4630–4638.

28 W. Fu, X. Y. Wang and Z. Q. Huang, Remarkable reusability of magnetic Fe₃O₄-encapsulated C₃N₃S₃ polymer/reduced graphene oxide composite: a highly effective adsorbent for Pb and Hg ions, *Sci. Total Environ.*, 2019, **659**, 895–904.

29 H. Lee, S. M. Dellatore, W. M. Miller and P. B. Messersmith, Mussel-inspired surface chemistry for multifunctional coatings, *Science*, 2007, **318**(5849), 426–430.

30 H. F. Chen, Y. Zhou, J. Y. Wang, J. Lu and Y. B. Zhou, Polydopamine modified cyclodextrin polymer as efficient adsorbent for removing cationic dyes and Cu²⁺, *J. Hazard. Mater.*, 2020, **389**, 121897.

31 Y. Z. Li, R. Zhao, S. Chao, B. L. Sun, C. Wang and X. Li, Polydopamine coating assisted synthesis of MnO₂ loaded inorganic/organic composite electrospun fiber adsorbent for efficient removal of Pb²⁺ from water, *Chem. Eng. J.*, 2018, **344**, 277–289.

32 T. Posati, M. Nocchetti, A. Kovtun, A. Donnadio, M. Zambianchi, A. Aluigi, M. L. Capobianco, F. Corticelli, V. Palermo, G. Ruani, R. Zamboni, M. L. Navacchia and M. Melucci, Polydopamine Nanoparticle-Coated Polysulfone Porous Granules as Adsorbents for Water Remediation, *ACS Omega*, 2019, **4**(3), 4839–4847.

33 H. Wang, C. C. Lin, X. R. Zhang, K. L. Lin, X. D. Wang and S. G. Shen, Mussel-Inspired Polydopamine Coating: A General Strategy To Enhance Osteogenic Differentiation and Osseointegration for Diverse Implants, *ACS Appl. Mater. Interfaces*, 2019, **11**(7), 7615–7625.

34 W. Y. Wang, Z. Tang, Y. Zhang, Q. X. Wang, Z. G. Liang and X. W. Zeng, Mussel-Inspired Polydopamine: The Bridge for Targeting Drug Delivery System and Synergistic Cancer Treatment, *Macromol. Biosci.*, 2020, **20**, 200022.

35 Z. S. Yan, Y. H. Zhang, H. Y. Yang, G. D. Fan, A. Ding, H. Liang, G. B. Li, N. Q. Ren and B. Van der Bruggen, Mussel-inspired polydopamine modification of polymeric membranes for the application of water and wastewater treatment: a review, *Chem. Eng. Res. Des.*, 2020, **157**, 195–214.

36 V. C. Mai, P. Das, J. J. Zhou, T. T. Lim and H. W. Duan, Mussel-Inspired Dual-Superlyophobic Biomass Membranes for Selective Oil/Water Separation, *Adv. Mater. Interfaces*, 2020, **7**(6), 1901756.

37 C. F. Ding, Y. L. Sun, Y. H. Wang, J. B. Li, Y. N. Lin, W. Y. Sun and C. N. Luo, Adsorbent for resorcinol removal based on cellulose functionalized with magnetic poly (dopamine), *Int. J. Biol. Macromol.*, 2017, **99**, 578–585.

38 X. F. Shu, H. D. Ren, Y. Jiang, J. Zhou, Y. Q. Wang, Y. F. Wang, Y. Liu and W. C. Oh, Enhanced electromagnetic absorption performance of silane coupling agent KH550@ Fe₃O₄ hollow nanospheres/graphene composites, *J. Mater. Chem. C*, 2020, **8**, 2913–2926.

39 S. Mallakpour and F. Motirasoul, Preparation of PVA/alpha-MnO₂-KH550 nanocomposite films and study of their morphology, thermal, mechanical and Pb(II) adsorption properties, *Prog. Org. Coat.*, 2017, **103**, 135–142.

40 P. P. Yang, Q. Liu, J. Y. Liu, R. R. Chen, R. M. Li, X. F. Bai and J. Wang, Highly efficient immobilization of uranium(VI) from aqueous solution by phosphonate-functionalized dendritic fibrous nanosilica (DFNS), *J. Hazard. Mater.*, 2019, **363**, 248–257.

41 D. B. Knorr, N. T. Tran, K. J. Gaskell, J. A. Orlicki, J. C. Woicik, C. Jaye, D. A. Fischer and J. L. Lenhart, Synthesis and Characterization of Aminopropyltriethoxysilane-Polydopamine Coatings, *Langmuir*, 2016, **32**(17), 4370–4381.

42 L. J. Cui, Y. Zhang and X. S. Zhao, Pollutants removal in subsurface constructed wetland based on the first-order kinetic model (In Chinese), *China Environ. Sci.*, 2011, **31**, 1697–1704.

43 A. A. Brennan, A. D. Harwood, J. You, P. F. Landrum and M. J. Lydy, Degradation of fipronil in anaerobic sediments



and the effect on porewater concentrations, *Chemosphere*, 2009, **77**(1), 22–28.

44 D. Baderna, S. Maggioni, E. Boriani, S. Gemma, M. Molteni, A. Lombardo, A. Colombo, S. Bordonali, G. Rotella and M. Lodi, A combined approach to investigate the toxicity of an industrial landfill's leachate: chemical analyses, risk assessment and in vitro assays, *Environ. Res.*, 2011, **111**(4), 603–613.

45 G. D. Barnes, Reference Dose (RfD): Description and Use in Health Risk Assessments, *Regul. Toxicol. Pharmacol.*, 1988, **8**(4), 471–486.

46 USEPA, *Exposure Factors Handbook*, Environmental Protection Agency, Office of Research and Development, Washington, DC, 1997.

47 G. S. S. Mamaril, M. D. G. de Luna, K. Bindumadhavan, D. C. Ong, J. A. I. Pimentel and R. Doong, Nitrogen and fluorine co-doped 3-dimensional reduced graphene oxide architectures as high-performance electrode material for capacitive deionization of copper ions, *Sep. Purif. Technol.*, 2021, **272**, 117559.

48 K. Z. Elwakeel, A. M. Elgarahy, Z. A. Khan, M. S. Almughamisi and A. S. Al-Bogami, Perspectives Regarding Metals/Minerals-Incorporated Materials for Water Purification: With Special Focus on Cr(VI) Removal, *Mater. Adv.*, 2020, **1**, 1546–1574.

49 S. S. Gupta and K. G. Bhattacharyya, Adsorption of metal ions by clays and inorganic solids, *RSC Adv.*, 2014, **4**, 28537–28586.

50 Y. L. Liu, K. L. Ai and L. H. Lu, Polydopamine and its derivative materials: synthesis and promising applications in energy, environmental, and biomedical fields, *Chem. Rev.*, 2014, **114**, 5057–5115.

51 H. Shi, Y. He, Y. Pan, H. H. Di, G. Y. Zeng, L. Zhang and C. L. Zhang, A modified mussel-inspired method to fabricate TiO_2 decorated superhydrophilic PVDF membrane for oil/water separation, *J. Membr. Sci.*, 2016, **506**, 60–70.

52 Y. Q. Zhan, S. M. Zhao, X. Y. Wan and S. J. He, Hierarchical Fe_3O_4 -derived organic/inorganic hybrids constructed by modified bio-inspired functionalization: efficient adsorbents for water-soluble methylene blue and mechanism, *J. Chem. Technol. Biotechnol.*, 2019, **94**, 1638–1650.

53 L. Zhou, Y. He, H. Shi, G. Q. Xiao, S. H. Wang, Z. Y. Li and J. Y. Chen, One-pot route to synthesize HNTs@PVDF membrane for rapid and effective separation of emulsion-oil and dyes from waste water, *J. Hazard. Mater.*, 2019, **380**, 120865.

54 J. K. Gao, H. Lei, Z. Han, Q. Shi, Y. Chen and Y. J. Jiang, Dopamine functionalized tannic-acid-templated mesoporous silica nanoparticles as a new sorbent for the efficient removal of Cu^{2+} from aqueous solution, *Sci. Rep.*, 2017, **7**, 45215.

55 W. W. Cui, P. Li, Z. M. Wang, S. L. Zheng and Y. Zhang, Adsorption study of selenium ions from aqueous solutions using MgO nanosheets synthesized by ultrasonic method, *J. Hazard. Mater.*, 2018, **341**, 268–276.

56 L. Cáceres-Jensen, J. Rodríguez-Becerra, J. Parra-Rivero, M. Escudéy, L. Barrientos and V. Castro-Castillo, Sorption kinetics of diuron on volcanic ash derived soils, *J. Hazard. Mater.*, 2013, **261**, 602–613.

57 K. Ouyang, C. Zhu, Y. Zhao, L. Wang, S. Xie and Q. Wang, Adsorption mechanism of magnetically separable Fe_3O_4 /graphene oxide hybrids, *Appl. Surf. Sci.*, 2015, **355**, 562–569.

58 H. Wang, X. Hu, Y. Guo, C. Qiu, S. Long, D. Hao, X. Cai, W. Xu, Y. Wang and Y. Liu, Removal of copper ions by few-layered graphene oxide nanosheets from aqueous solutions: external influences and adsorption mechanisms, *J. Chem. Technol. Biotechnol.*, 2018, **93**, 2447–2455.

59 M. Adeli, Y. Yamini and M. Faraji, Removal of copper, nickel and zinc by sodium dodecyl sulphate coated magnetite nanoparticles from water and wastewater samples, *Arabian J. Chem.*, 2017, **10**, S514–S521.

60 J. A. V. Rodrigues, L. R. Martins, L. M. Furtado, A. L. P. Xavier, F. T. R. de Almeida, A. Moreira, T. M. S. Melo, L. F. Gil and L. V. A. Gurgel, Oxidized Renewable Materials for the Removal of Cobalt(II) and Copper(II) from Aqueous Solution Using in Batch and Fixed-Bed Column Adsorption, *Adv. Polym. Technol.*, 2020, **2020**, 17.

61 N. Temnuch, A. Suwattanamala, S. Inpaeng and K. Tedsree, Magnetite nanoparticles decorated on multi-walled carbon nanotubes for removal of Cu^{2+} from aqueous solution, *Environ. Technol.*, 2020, **42**, 1–28.

62 J. Li, S. W. Zhang, C. L. Chen, G. X. Zhao, X. Yang, J. X. Li and X. K. Wang, Removal of $\text{Cu}(\text{II})$ and Fulvic Acid by Graphene Oxide Nanosheets Decorated with Fe_3O_4 Nanoparticles, *ACS Appl. Mater. Interfaces*, 2012, **4**(9), 4991–5000.

63 J. N. Nkoh, R. K. Xu, J. F. Yan, J. Jiang, J. Y. Li and M. A. Kamran, Mechanism of $\text{Cu}(\text{II})$ and $\text{Cd}(\text{II})$ immobilization by extracellular polymeric substances (*Escherichia coli*) on variable charge soils, *Environ. Pollut.*, 2019, **247**, 136–145.

64 G. Zeng, Y. He, Y. Zhan, L. Zhang, Y. Pan, C. Zhang and Z. Yu, Novel polyvinylidene fluoride nanofiltration membrane blended with functionalized halloysite nanotubes for dye and heavy metal ions removal, *J. Hazard. Mater.*, 2016, **317**, 60–72.

65 J. K. Gao, H. Lei, Z. Han, Q. Shi, Y. Chen and Y. J. Jiang, Dopamine functionalized tannic-acid-templated mesoporous silica nanoparticles as a new sorbent for the efficient removal of Cu^{2+} from aqueous solution, *Sci. Rep.*, 2017, **7**, 45215.

66 M. Danish, R. Hashim, M. M. N. Ibrahim, M. Rafatullah, O. Sulaiman, T. Ahmad, M. Shamsuzzoha and A. Ahmad, Sorption of Copper(II) and Nickel(II) Ions from Aqueous Solutions Using Calcium Oxide Activated Date (Phoenix dactylifera) Stone Carbon: Equilibrium, Kinetic, and Thermodynamic Studies, *J. Chem. Eng. Data*, 2011, **56**(9), 3607–3619.

67 Y. L. Wang, S. Liang, B. D. Chen, F. F. Guo, S. L. Yu and Y. L. Tang, Synergistic Removal of $\text{Pb}(\text{II})$, $\text{Cd}(\text{II})$ and Humic Acid by Fe_3O_4 @Mesoporous Silica-Graphene Oxide Composites, *PLoS One*, 2013, **8**, 1–8.



68 H. Li, Y. Y. Zhao, Y. Jia, G. Chen, J. X. Peng and J. B. Li, pH-Responsive Dopamine-Based Nanoparticles Assembled via Schiff Base Bonds for Synergistic Anticancer Therapy, *Chem. Commun.*, 2020, **56**, 13347–13350.

69 J. Y. Wu, J. Chen, Y. J. Feng, S. J. Zhang, L. Lin, Z. P. Guo, P. J. Sun, C. N. Xu, H. Y. Tian and X. S. Chen, An immune cocktail therapy to realize multiple boosting of the cancer-immunity cycle by combination of drug/gene delivery nanoparticles, *Sci. Adv.*, 2020, **6**, 1–13.